

# Thermal Deformation Behavior of Ti-6Mo-5V-3Al-2Fe Alloy

Lin Han <sup>1</sup>, Haoyu Zhang <sup>1,\*</sup>, Jun Cheng <sup>2</sup>, Ge Zhou <sup>1</sup>, Chuan Wang <sup>1,3</sup> and Lijia Chen <sup>1</sup>

<sup>1</sup> College of Materials Science and Engineering, Shenyang University of Technology, Shenyang 110870, China; hanlin7922@163.com (L.H.); zhouge@sut.edu.cn (G.Z.); wangchuan@lnu.edu.cn (C.W.); chenlijia@sut.edu.cn (L.C.)

<sup>2</sup> Northwest Institute for Nonferrous Metal Research, Xi'an 710016, China; chengjun\_851118@126.com

<sup>3</sup> College of Light Industry, Liaoning University, Shenyang 110036, China

\* Correspondence: zhanghaoyu@sut.edu.cn

**Abstract:** The Gleeble-3800 thermal simulation machine was used to perform hot compression experiments on a new type of  $\beta$  alloy, Ti-6Mo-5V-3Al-2Fe (wt.%), at temperatures of 700–900 °C, strain rates of  $5 \times 10^{-1}$  to  $5 \times 10^{-4} \text{ s}^{-1}$ , and total strain of 0.7. Transmission and EBSD techniques were used to observe the microstructure. The results show that the deformation activation energy of the alloy was 356.719 KJ/mol, and dynamic recrystallization occurred during the hot deformation. The higher the deformation temperature was, the more obvious the dislocations that occurred and the more sufficient the dynamic recrystallization that occurred, but the effect of strain rate was the opposite. When the deformation temperature was higher than the phase transition point, the recrystallized grains clearly grew up. The calculated strain rate sensitivity index of the alloy was 0.14–0.29. The constitutive equation of hot deformation of Ti-6Mo-5V-3Al-2Fe alloy was established by using the Arrhenius hyperbolic sine equation. The dynamic DMM hot working diagram with the strain of 0.7 was constructed. The relatively good hot working area of the alloy was determined to be the deformation temperature of 700–720 °C and  $0.0041\text{--}0.0005 \text{ s}^{-1}$ .

**Keywords:** thermal compression; dynamic recrystallization; Arrhenius constitutive equation; thermal processing diagram



**Citation:** Han, L.; Zhang, H.; Cheng, J.; Zhou, G.; Wang, C.; Chen, L. Thermal Deformation Behavior of Ti-6Mo-5V-3Al-2Fe Alloy. *Crystals* **2021**, *11*, 1245. <https://doi.org/10.3390/cryst11101245>

Academic Editors: Sergio Brutti and Shujun Zhang

Received: 17 September 2021

Accepted: 9 October 2021

Published: 14 October 2021

**Publisher's Note:** MDPI stays neutral with regard to jurisdictional claims in published maps and institutional affiliations.



**Copyright:** © 2021 by the authors. Licensee MDPI, Basel, Switzerland. This article is an open access article distributed under the terms and conditions of the Creative Commons Attribution (CC BY) license (<https://creativecommons.org/licenses/by/4.0/>).

## 1. Introduction

Titanium alloy has been widely used in aerospace and other fields because of its advantages such as high density and low strength [1–4]. Metastable  $\beta$  titanium alloys are mainly used to make structural parts, and therefore their mechanical properties are critical [5]. After solid solution and aging, its strength can be significantly improved through precipitation strengthening, but its plasticity is often poor [6,7]. One of the reasons for this phenomenon is that the  $\beta$  grains are too coarse [8].  $\beta$  grain size in metastable  $\beta$  titanium alloy is subject to internal softening mechanisms such as dynamic recovery and dynamic recrystallization during hot working. Therefore, it is very necessary to study the thermal deformation behavior of metastable  $\beta$  titanium alloy for its future development.

Ouyang et al. [9] conducted hot compression experiments on the  $\beta$  phase region of forged TB6 titanium alloy. It was found that dynamic recrystallization is the hot deformation mechanism of TB6 alloy, and the main nucleation mechanism of new recrystallized grains is arch bending nucleation. Fan et al. [10] conducted thermal compression experiments on Ti-7333 alloy at different temperatures and found that the dominant mechanism of microstructure changes during thermal compression is dynamic recovery, spheroidization, and dynamic recrystallization. Dynamic recrystallization would become more apparent with the increase of deformation temperature and the decrease of deformation rate. The main factors affecting the thermal deformation behavior of materials are deformation temperature, strain rate, and deformation amount. Flow stress and hot working parameters can be related and described by a constitutive equation. Zhu et al. [11] conducted

high-temperature compression experiments on TB17 and established constitutive equations under certain conditions. Aneta [12] systematically studied the Ti-3Al-8V-6Cr-4Zr-4Mo alloy with a hot working diagram. She established the hot working diagram using a dynamic material model (DMM) to accurately describe the steady-state and unsteady-state regions of the alloy during high-temperature deformation. It was seen that different metastable  $\beta$  alloys exhibited different thermal deformation behaviors under different conditions.

Ti-6Mo-5V-3Al-2Fe alloy is a new type of metastable  $\beta$  titanium alloy. In previous studies, it has been found that the tensile strength of the alloy can reach more than 1500 MPa after solution and aging treatment [13]. As a new type of  $\beta$  titanium alloy, its hot deformation behavior during hot working is still unclear. In this paper, the dynamic recrystallization behavior of Ti-6Mo-5V-3Al-2Fe alloy under different states was analyzed in combination with the characteristics of the actual stress–true strain curve during the hot compression process, and the constitutive equation and hot working diagram were established. The deformation mechanism and the rheological instability region during the hot deformation of the alloy were analyzed.

## 2. Materials and Methods

Ti-6Mo-5V-3Al-2Fe alloy comprises grade 0 sponge titanium, pure molybdenum powder, V-Al master alloy, pure iron, and aluminum foil. The alloy elements were placed in proportion and poured into the aluminum foil to form an alloy package. The elements were added to the alloy in smaller particle sizes. The prepared alloy package and titanium sponge were put into a hydraulic press mold for pre-densification. Then, a cylindrical electrode rod with 50 mm diameter and 180 mm height was prepared. The electrode rod was smelted into an alloy ingot by a vacuum consumable electric arc furnace. (Liaoning Jinzhou Transformer Circuit Factory, Jinzhou city, China). The purpose of repeating it twice was to ensure that the composition of the ingot was uniform. We then took three samples from the alloy ingot and measured the element content of the alloy ingot on an X-ray fluorescence spectrometer. The deviation of the alloy ingot element content from the nominal composition was within the allowable range. The Ti-6Mo-5V-3Al-2Fe alloy was prepared through arc melting, and the detailed chemical composition is listed in Table 1. The  $\beta$ -transus temperature of the Ti-6Mo-5V-3Al-2Fe alloy was 815 °C, measured by the metallographic method. The average grain size of the alloy before deformation was about 150  $\mu$ m, as shown in Figure 1.

**Table 1.** Composition of Ti-6Mo-5V-3Al-2Fe alloy.

Composition	Mo	V	Al	Fe	C	N	H	O
Content	6.230	5.290	2.980	1.930	0.019	0.030	0.002	0.07

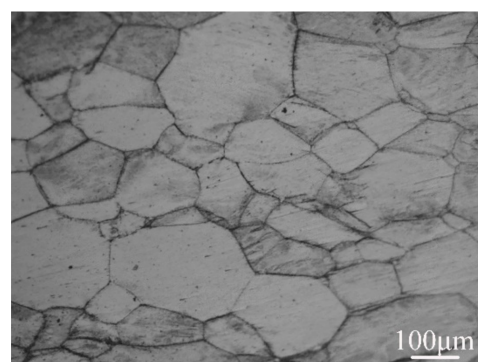


**Figure 1.** Microstructure of Ti-6Mo-5V-3Al-Fe alloy before hot compression.

The sample used in the thermal simulation compression experiment was a cylindrical sample cut from the Ti-6Mo-5V-3Al-2Fe alloy billet. The sample size was 10 mm in diameter

and 15 mm in height, and the surface was polished with sandpaper until it was bright; then, the surface was removed to eliminate the scale and machining marks. At the same time, it was ensured that the end, the face of the sample was perpendicular to the axis of the sample.

The temperatures were 700, 750, 800, 850, and 900 °C; the strain rates were  $5 \times 10^{-1}$ ,  $5 \times 10^{-2}$ ,  $5 \times 10^{-3}$  and  $5 \times 10^{-4} \text{ s}^{-1}$ , and the total strain was 0.7. The thermal simulation experiment was carried out with the Gleeble-3800 thermal simulation experimental machine.

Graphite is placed at both ends of the sample to reduce the friction between the indenter and the sample; a thermocouple was placed on the surface of the sample to feedback the surface temperature change of the sample. This test adopted resistance heating; the heating rate was 10 °C/s, the holding time was 3 min, and the cooling method was water cooling. The TEM specimens with 3 mm diameter and 0.5 mm thickness were cut from the specimens after hot deformation. The EBSD specimens with 8 mm length, 8 mm width, and 3 mm height were cut from the specimens after hot deformation. After sandpaper grinding, electrolytic polishing and double spray were carried out. The liquid electrolyte of double spray was  $\text{HClO}_4:\text{C}_4\text{H}_9\text{O}_3:\text{CH}_3\text{O}_3 = 6:34:60$ . Nordlys Nano EBSD detector was used to observe the recrystallized grain distribution, orientation, and grain boundary morphology of the original grain after hot deformation. The JEM-2100 transmission electron microscope observed the internal dislocation configuration of the alloy.

### 3. Results

#### 3.1. True Stress-True Strain Curve

Figure 2 shows the true stress–true strain lines of Ti-6Mo-5V-3Al-2Fe alloy at the temperature of 700–900 °C and the strain rates of  $5 \times 10^{-1}$  to  $5 \times 10^{-4} \text{ s}^{-1}$ . As shown in the figure, the flow stress was affected by deformation temperature and strain rate [14]. At the initial stage of deformation, the true stress increased rapidly, and the curve slope was large. The main reason was that the work hardening occurred inside the alloy, which led to the increase of dislocation density and dislocation plug, as well as the rapid increase of flow stress. With the increase of strain, a softening mechanism appeared in the alloy, leading to the gradual flattening of the curve. With the continuous increase of strain, the effect of flow softening on the curvature of the alloy was increased, the curve declined, and the flow stress decreased gradually until the balance of work hardening and flows softening was reached, wherein the slope of the curve almost no longer changed [15,16].

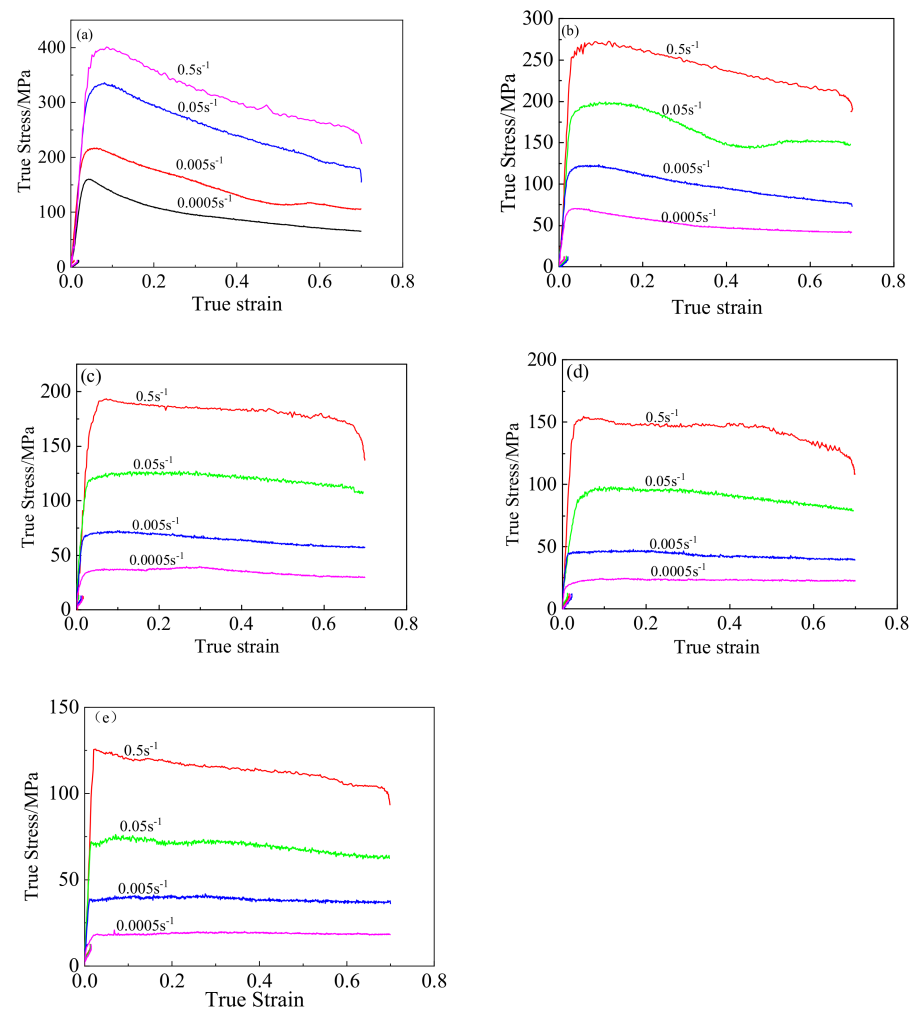
#### 3.2. Effect of Hot Deformation Parameters on Alloy Microstructure

Thermal deformation parameters such as deformation temperature and strain rate affect the thermal compression process of metals. When the alloy temperature is higher than the recrystallization temperature, plastic deformation and hardening occur inside the material, and two opposite deformations occur in the alloy.

As the strain rate increases, the grain size decreases, and the dislocation density does not change significantly.

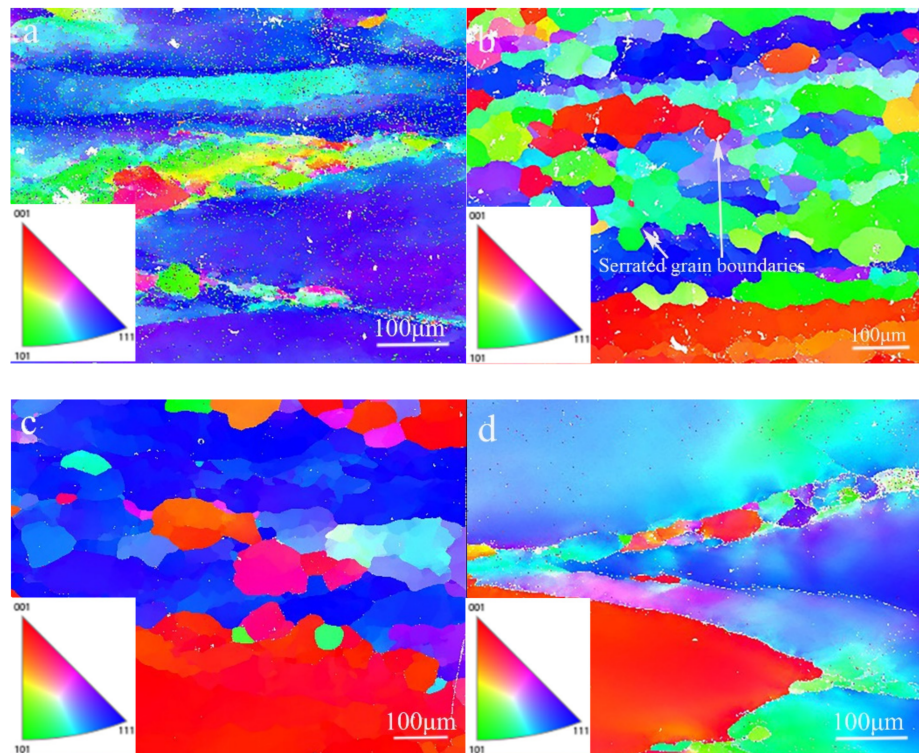
##### 3.2.1. Influence of Deformation Temperature

Figure 3a–c shows the EBSD diagram at the strain rate of  $0.0005 \text{ s}^{-1}$  and temperatures of 750, 800, and 850 °C. Dynamic recrystallization existed at 750 °C, but the degree was low, and dynamic recrystallization occurred obviously at 800 °C and 850 °C. However, the high temperature made the recrystallized grain size grow significantly, and the coarse equiaxed  $\beta$  grain was formed, but the effect on the microstructure refinement was not apparent.



**Figure 2.** True stress–true strain curves of Ti-6Mo-5V-3Al-2Fe alloy at different temperatures: 700 °C (a), 750 °C (b), 800 °C (c), 850 °C (d), and 900 °C (e).

Figure 4a,b shows TEM structures of the alloy at the different deformation temperatures. It can be seen that the  $\beta$  matrix had deformation and dynamic recrystallization substructures. As shown in Figure 4a, when the deformation temperature was 750 °C, there were a large number of  $\alpha$  phases existing in the  $\beta$  matrix because the deformation temperature was below the  $\beta$ -transus temperature. During deformation, the dislocation slip was hindered by  $\alpha$  phase. As shown in Figure 4b, at 800 °C, the dislocations were mainly located at grain boundaries and the deformation induced a large number of dislocations. The  $\beta$  grains were composed of many parallel dislocation bands, showing a mixture of deformation and polygons. In other places, dynamic recrystallization occurred. Therefore, grain size and dislocation density increased with increasing temperature.



**Figure 3.** Grain orientation distribution of Ti-6Mo-5V-3Al-2Fe alloy under different conditions of hot compression: 750 °C 0.0005 s<sup>-1</sup> (a), 800 °C 0.0005 s<sup>-1</sup> (b), 850 °C 0.0005 s<sup>-1</sup> (c), and 800 °C 0.5 s<sup>-1</sup> (d).

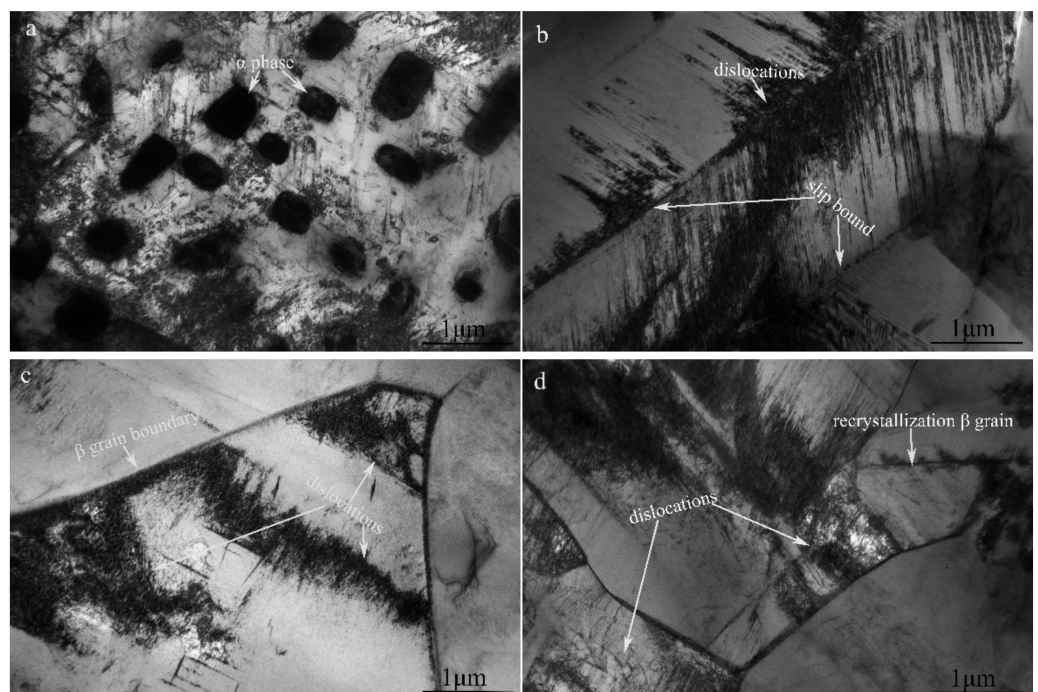


**Figure 4.** TEM of Ti-6Mo-5V-3Al-2Fe alloy under different deformation conditions: 750 °C 0.0005 s<sup>-1</sup> (a), 800 °C 0.0005 s<sup>-1</sup> (b), 850 °C 0.0005 s<sup>-1</sup> (c), and 850 °C 0.5 s<sup>-1</sup> (d).

### 3.2.2. Effect of Strain Rate

When the temperature is constant, the higher the strain rate, the higher the energy storage, the higher the driving force of dynamic recrystallization, the more the recrystallized

grains, but the short deformation time leads to the insufficient growth of recrystallized grains [17,18].

Figure 3b,d shows the EBSD diagram at the temperature of 800 °C and strain rate of 0.0005 s<sup>-1</sup>. When the strain rate was 0.0005 s<sup>-1</sup>, the dynamic recrystallization degree was high. Because of the long deformation time, the recrystallized grains were fully grown, and the grain boundaries appeared serrated. At 0.5 s<sup>-1</sup>, although the degree of dynamic recrystallization was high, the deformation time was relatively short, and the recrystallization development was not sufficient. The fine recrystallization grains mainly occurred near the grain boundary, and the grain boundary will fluctuate due to the incongruity of the plastic deformation of the two grains. The fluctuating part will hinder the slip and shear of grain boundary, and therefore many dislocations will gather here and become the nucleation core of recrystallization [19]. The original  $\beta$  grains were elongated, and the dynamically recrystallized grains were distributed in a chain pattern around the original grain boundary [20].

Figure 4c,d shows the TEM structures of the alloy at the different strain rates.

At the strain rate under the condition of 0.0005 s<sup>-1</sup>, a large number of dislocations were formed in the microstructure. In the process of slippage and climbing, dislocations gathered, tangled, canceled, and rearranged each other to form cellular substructures. The cellular structure of the merger grew up in a tiny grain boundary. Near the grain boundary adsorption of dislocation, dynamic recrystallization occurred in the organization. Under the condition of 0.5 s<sup>-1</sup> strain rate, the thermal deformation time was short, a large number of dislocation slips and climbing time were insufficient, and the recrystallized grains were tiny. The strain rate increased, the grain size decreased, and the dislocation density did not change significantly.

### 3.3. Strain Rate Sensitivity Index

Backofen [21] established the deformation exponential equation  $\sigma = K\dot{\epsilon}^m$ , where the flow stress  $\sigma$  is associated with the strain rate  $\dot{\epsilon}$ .  $K$  is a constant determined by the material, and  $m$  is the strain rate sensitivity index. By differentiating it, we obtain  $m = d\lg\sigma/d\lg\dot{\epsilon}$ . The  $\lg\sigma$ - $\lg\dot{\epsilon}$  impartiality curve at true strain-true strain uniform deformation, slope  $m$ , was made, as shown in Figure 5. As the temperature increased, the increase of  $m$  value was close to 0.3, indicating that the alloy had good superplasticity, as shown in Table 2.

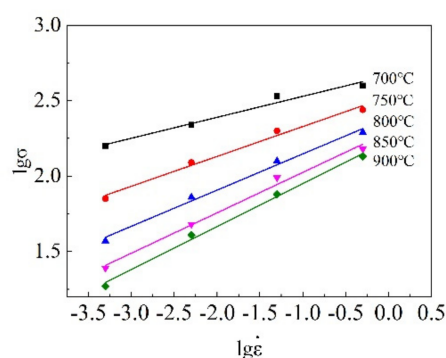


Figure 5.  $\lg\sigma$ - $\lg\dot{\epsilon}$  curve of Ti-6Mo-5V-3Al-2Fe alloy at different temperatures.

Table 2. The  $m$  value of Ti-6Mo-5V-3Al-2Fe alloy at different temperatures ( $\epsilon = 0.7$ ).

$T, ^\circ\text{C}$	700	750	800	850	900
$M$ value	0.14	0.2	0.24	0.27	0.29

### 3.4. Constitutive Equation Based on Arrhenius Formula

The essence of studying the thermal deformation of materials is changing the thermal activation energy affected by the thermal deformation parameters. The relationship

between strain rate, deformation temperature, and flow stress can be expressed by the Arrhenius constitutive equation as follows [22–24]:

$$\dot{\epsilon} = A_1 \sigma^n \exp(-Q/RT) \quad (1)$$

$$\dot{\epsilon} = A_2 \exp(\beta\sigma) \exp(-Q/RT) \quad (2)$$

$$\dot{\epsilon} = A_3 \sinh(\alpha\sigma)^n \exp(-Q/RT) \quad (3)$$

Among them,  $A_1 A_2 A_3$ ,  $\alpha$ , and  $\beta$  are the material constants;  $Q$  is the deformation activation energy (J/mol);  $n$  is the stress index;  $R$  is the gas constant of 8.314 J/(mol·K); and  $T$  is the absolute temperature (K). When the flow stress is low ( $\alpha\sigma < 0.8$ ), it is expressed by Equation (1); when the flow stress is high ( $\alpha\sigma > 1.2$ ), it is expressed by Equation (2); and Equation (3) applies to all situations. Therefore, this experiment used the Arrhenius hyperbolic sine equation to establish the constitutive equation. We found the true stress–true strain curve peak  $\sigma$  corresponding to different temperatures and strain rates, determined the relationship between  $\ln\dot{\epsilon}$ – $\sigma$  and  $\ln\dot{\epsilon}$ – $\ln\sigma$  as shown in Figure 6. and performed linear fitting on the curve to obtain  $n = 4.68462$  and  $\beta = 0.04269$ . According to  $\alpha = \beta/n$ ,  $\alpha = 0.00911 \text{ MPa}^{-1}$ .

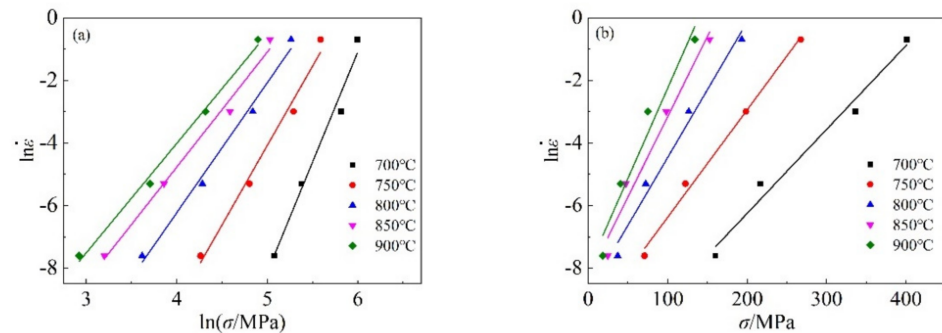


**Figure 6.** Relation diagram of strain rate and flow stress of Ti-6Mo-5V-3Al-2Fe alloy under strain 0.7  $\ln\dot{\epsilon}$ – $\sigma$  curve (a) and  $\ln\dot{\epsilon}$ – $\ln\sigma$  curve (b).

We took the logarithm of Equation (3) to obtain

$$\ln \dot{\epsilon} = \ln A + n \ln[\sinh(\alpha\sigma)] - Q/RT \quad (4)$$

For Equation (4) partial differentiation, we obtained

$$Q = R \cdot \left[ \frac{\partial \ln \sinh(\alpha\sigma)}{\partial \left(\frac{1}{T}\right)} \right] \cdot \left[ \frac{\partial \ln \dot{\epsilon}}{\partial \ln \sinh(\alpha\sigma)} \right] \quad (5)$$

We brought the calculated  $\alpha$  and different temperatures and strain rates into (5) to produce  $\partial \ln \sinh(\alpha\sigma) / \partial (1/T)$  and  $\partial \ln \dot{\epsilon} / \partial \ln \sinh(\alpha\sigma)$  as shown in Figure 7. With regards to the relation curve graph, we found its corresponding slope after linear fitting. The corresponding average slopes were 3.149104 and 13.62476, and the average  $Q = 356.719 \text{ KJ/mol}$  can be obtained by taking them into Equation (5).

Since  $\alpha$ -Ti diffusion activation energy  $Q = 242 \text{ KJ/mol}$ ,  $\beta$ -Ti self-diffusion activation energy  $Q = 153 \text{ KJ/mol}$  [25]. It is generally believed that when the activation energy of titanium alloy deformation is very different from the activation energy of self-diffusion, the softening mechanism may be dynamic recrystallization.

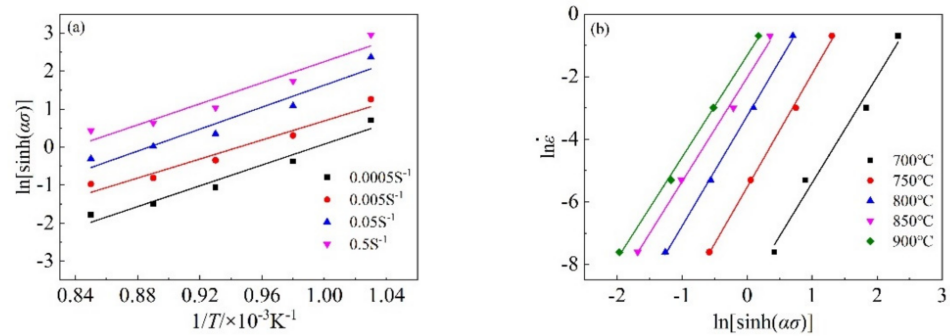


**Figure 7.** Relationship between flow stress and thermal deformation parameters of Ti-6Mo-5V-3Al-2Fe alloy at strain 0.7  $\ln[\sinh(\alpha\sigma)] - \partial \ln \dot{\epsilon} - \partial \ln \sinh(\alpha\sigma)$  curve (a) and  $\partial \ln \dot{\epsilon} - \partial \ln \sinh(\alpha\sigma)$  curve (b).

Zener and Hollomon [26] proposed the Zener–Hollomon parameter, which represents the strain rate factor of temperature compensation, namely, parameter  $Z$ , and its expression is

$$Z = \dot{\epsilon} \exp(Q/RT) = A[\sinh(\alpha\sigma)]^n \quad (6)$$

When the strain rate is constant, assuming that the deformation activation energy remains constant within a specific temperature range, the logarithm of both sides of the equation is taken to obtain.

$$\ln Z = \ln \dot{\epsilon} + Q/RT = \ln A + n \ln[\sinh(\alpha\sigma)] \quad (7)$$

The deformation activation energy  $Q$  and different temperature strain rates are brought into Equation (7) to calculate different  $\ln Z$  values, making a linear fitting of the  $\ln[\sinh(\alpha\sigma)] - \ln Z$  curve relationship as shown in Figure 8. The slope of the fitting straight line is  $n = 3.0082$  and the intercept is  $\ln A = 35.14482$ , with  $A$  being obtained as  $e^{35.14482}$ .

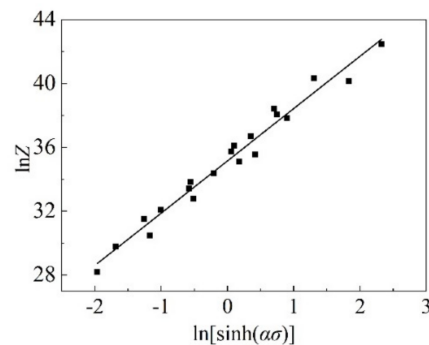


**Figure 8.**  $\ln[\sinh(\alpha\sigma)] - \ln Z$  diagram of Ti-6Mo-5V-3Al-2Fe alloy at strain 0.7.

In summary, the Arrhenius constitutive equation of Ti-6Mo-5V-3Al-2Fe alloy at a temperature of 700–900 °C with a strain rate of  $5 \times 10^{-1}$  to  $5 \times 10^{-4} \text{ s}^{-1}$  and a total strain of 0.7 is  $\dot{\epsilon} = e^{35.14482} [\sinh(0.00911\sigma)]^{3.0082} \exp(-356.719/RT)$ .

### 3.5. Thermal Processing Map

The theoretical basis of the dynamic materials model (DMM) is strong plastic continuum mechanics, physical system model, and irreversible thermodynamics [27]. The plastic deformation process can be regarded as an energy dissipation system, and the energy consumption depends on the material-processing rheological behavior. Under a specific strain rate, the energy  $P$  used by the material to absorb plastic deformation mainly includes two parts. One is dissipation ( $G$ ), which refers to the energy consumed by the material

undergoing plastic deformation. The other is the dissipation co-quantity ( $J$ ) refers to the energy dissipated by the change of the structure during the deformation of the material.

$$P = J + G \quad P = \sigma \bullet \dot{\epsilon} = \int_0^{\dot{\epsilon}} \sigma \bullet d\dot{\epsilon} + \int_0^{\sigma} \dot{\epsilon} \bullet d\sigma \quad (8)$$

The material's rheological properties determine the distribution between the dissipation factor and the dissipation factor, and the ratio of the dissipation factor and the dissipation factor is the strain rate sensitivity index  $m$ , that is,  $m = \frac{dJ}{dG} = \left( \frac{\partial(\log \sigma)}{\partial(\log \dot{\epsilon})} \right)_{\epsilon, T}$ .

Under specific temperature and strain,  $J = \int_0^{\sigma} \dot{\epsilon} \bullet d\sigma = \sigma \bullet \dot{\epsilon} \frac{m}{m+1}$ . When  $m = 1$ ,  $J$  reaches the maximum value,  $J_{\max} = \frac{\sigma \dot{\epsilon}}{2}$ , power dissipation rate  $\eta = \frac{J}{J_{\max}} = \frac{2m}{m+1}$ .

The true strain is selected as the flow stress value of the thermal compression experiment under different temperature and strain rates at 0.7. The cubic spline interpolation function is used to fit the functional relationship between  $\ln \sigma$  and  $\ln \dot{\epsilon}$ :  $\ln \sigma = a + b \ln \dot{\epsilon} + c \ln (\ln \dot{\epsilon})^2 + d (\ln \dot{\epsilon})^3$ . The partial derivative of  $\ln$  on both sides of the equation simultaneously yields  $m = \frac{d \ln \sigma}{d \ln \dot{\epsilon}} = b + 2c \ln \dot{\epsilon} + 3d (\ln \dot{\epsilon})^2$ , calculating the  $m$  value and  $\eta$  value of the thermal compression experiment under different conditions.

Prasad et al. [28] found that the power dissipation  $D$  and the strain rate  $\dot{\epsilon}$  satisfy the inequality:  $\frac{\partial D}{\partial \dot{\epsilon}} < \frac{D}{\dot{\epsilon}}$ , in order to study whether the area is stable or not. According to the DMM,  $D$  is the dissipation factor  $J$ . In order for the alloy instability area to be obtained, the expression is replaced with the strain rate sensitivity index  $m$  and the strain rate  $\dot{\epsilon}$  to express

$$\xi(\dot{\epsilon}) = \frac{\partial \ln \left[ \frac{m}{m+1} \right]}{\partial \ln \dot{\epsilon}} + m < 0 \quad (9)$$

With the temperature strain rate taken as the XY axis, the contour map is drawn with  $\xi(\dot{\epsilon}) < 0$  as the instability map. The energy dissipation map is superimposed on the instability map, which is the Ti-6Mo-5V-3Al-2Fe alloy hot working diagram. Figure 9 is the processing diagram of Ti-6Mo-5V-3Al-2Fe alloy at a strain of 0.7. There are two rheological instability regions, namely, 720–800 °C 0.06–0.5 s<sup>-1</sup> and 840–900 °C 0.007–0.5 s<sup>-1</sup>; the maximum value of  $\eta$  in the steady-state area appears in the 700–720 °C 0.0041–0.0005 s<sup>-1</sup> area, and the corresponding maximum power dissipation rate value is 0.52.

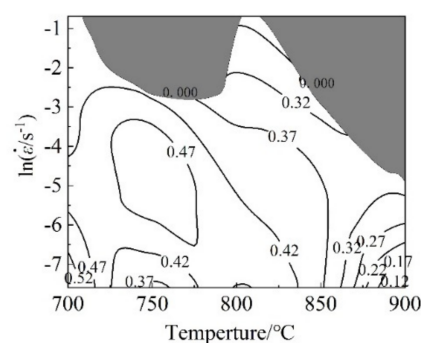


Figure 9. Hot working diagram of Ti-6Mo-5V-3Al-2Fe alloy.

#### 4. Conclusions

(1) The deformation activation energy of Ti-6Mo-5V-3Al-2Fe alloy was 356.719 KJ/mol at a certain temperature and strain rate range, which proved that dynamic recrystallization occurred in the alloy during hot deformation.

(2) The Arrhenius formula constitutive equation is  $\dot{\epsilon} = e^{35.14482} [\sinh(0.00911\sigma)]^{3.0082} \exp(-356.719/RT)$ .

(3) The rheological instability zone of the Ti-6Mo-5V-3Al-2Fe alloy was 0.06–0.5 s<sup>-1</sup> at 720–800 °C and 0.007–0.5 s<sup>-1</sup> at 840–900 °C. The steady-state deformation zone was 700–720 °C, 0.0041–0.0005 s<sup>-1</sup>.

**Author Contributions:** Conceptualization, L.H. and H.Z.; methodology, G.Z.; software, J.C.; data curation, C.W.; writing—original draft preparation, L.C.; writing—review and editing, L.H. All authors have read and agreed to the published version of the manuscript.

**Funding:** National Natural Science Foundation of China (52104379), Liaoning Provincial Department of Education Young Science and Technology Talents “Seedling” Project (LQGD2020012), Shaanxi Province Key Research and Development Plan (2020GY-251) and Science and Technology Project of Xi’an (2020KJRC0141).

**Data Availability Statement:** Not applicable.

**Conflicts of Interest:** The authors declare no conflict of interest.

## References

1. Zhang, Y.; Wang, F.K.; Qu, D. High temperature deformation behavior of Ti-4.5Al-6.5Mo-2Cr-2.6Nb-2Zr-1Sn titanium alloy. *Rare Metal Mater. Eng.* **2020**, *49*, 944–949.
2. Williams, J.C.; Starke, E.A. Progress in structural materials for aerospace system. *Acta Mater.* **2003**, *51*, 5775–5799. [[CrossRef](#)]
3. Jones, N.G.; Jackson, M. On mechanism of flow softening in Ti-5Al-5Mo-5V-3Cr. *Mater. Sci. Tech-Lond.* **2011**, *27*, 1025–1032. [[CrossRef](#)]
4. Yan, M.Q.; Chen, L.Q.; Yang, P.; Huang, L.J.; Tong, J.B.; Li, H.F.; Guo, P.D. Effect of hot deformation parameters on the evolution of microstructure and texture of beta Phase in TC18 Titanium Alloy. *Acta Metall. Sin.* **2021**, *57*, 880–890.
5. Lv, Y.P.; Li, S.J.; Zhang, X.Y.; Chen, C.; Zhou, K.C. Effects of strain rate on grain boundary evolution in Ti-55531 alloy. *Mater. Sci. Tech-Lond.* **2018**, *34*, 1880–1886. [[CrossRef](#)]
6. Ren, L.; Xiao, W.L.; Chang, H.; Zhang, Y.Q.; Ma, C.L.; Zhu, L. Microstructural tailoring and mechanical properties of a multi-alloyed near  $\beta$  titanium alloy Ti-5321 with various heat treatment. *Mater. Sci. Eng. A* **2018**, *711*, 553–561. [[CrossRef](#)]
7. Wang, P.Y.; Zhang, H.Y.; Zhang, Z.P.; Sun, J.; Xie, G.M.; Cheng, J.; Chen, L.J. Effect of solution temperature on the microstructure and tensile properties of metastable  $\beta$  titanium alloy Ti-4Mo-6Cr-3Al-2Sn. *Chin. J. Mater. Res.* **2020**, *34*, 473–480.
8. Shang, G.Q.; Kou, H.C.; Fei, Y.; Chang, H.; Zhu, Z.S.; Wang, X.N.; Zhang, F.S.; Li, J.S. Influence of aging processing on microstructure and mechanical properties of Ti-10V-2Fe-3Al alloy. *Rare Metal Mater. Eng.* **2021**, *39*, 1061–1065.
9. Ouyang, D.L.; Cui, X.; Lu, S.Q.; Xu, Y. Compression deformation behavior and dynamic recrystallization in  $\beta$  phase region of forged TB6 titanium alloy. *Chin. J. Mater. Res.* **2019**, *33*, 218–224.
10. Fan, J.K.; Kou, H.C.; Lai, M.J.; Tang, B.; Chang, H.; Li, S.J. Hot deformation mechanism and microstructure evolution of a new near  $\beta$  titanium alloy. *Mater. Sci. Eng. A* **2013**, *584*, 121–132. [[CrossRef](#)]
11. Zhu, H.C.; Luo, J.M.; Zhu, Z.S. High temperature compression deformation behavior of TB17 titanium alloy. *J. Aeronaut. Mater.* **2019**, *39*, 44–52.
12. Łukaszek-Sołek, A.; Krawczyk, J. The analysis of the hot deformation behaviour of the Ti-3Al-8V-6Cr-4Zr-4Mo alloy, using processing maps, a map of microstructure and of hardness. *Mater. Des.* **2015**, *65*, 165–173. [[CrossRef](#)]
13. Zhang, H.Y.; Li, X.H.; Lin, L.; Zhang, S.Q.; Wang, C.; Chen, L.J. Effect of aging temperature on microstructural evolution and mechanical properties in a novel  $\beta$  titanium alloy. *Rare Metal Mater. Eng.* **2019**, *48*, 3812–3818.
14. Zhang, S.; Zeng, W.; Zhou, D.; Lai, Y. Hot workability of burn resistant Ti-35V-15Cr-0.3Si-0.1C alloy. *Mater. Sci. Tech-Lond.* **2016**, *32*, 915–922. [[CrossRef](#)]
15. Yang, J.L.; Wang, G.F.; Jiao, X.Y.; Li, Y.; Liu, Q. High-temperature deformation behavior of the extruded Ti-22Al-25Nb alloy fabricated by powder metallurgy. *Mater. Charact.* **2018**, *137*, 170–179. [[CrossRef](#)]
16. Fan, J.K.; Kou, H.C.; Lai, M.J.; Tang, B.; Chang, H.; Li, J.S. Characterization of hot deformation behavior of a new near beta titanium alloy: Ti-7333. *Mater. Des.* **2013**, *49*, 945–952. [[CrossRef](#)]
17. Matsumoto, H.; Kitamura, M.; Li, Y.; Koizumi, Y.; Chiba, A. Hot forging characteristic of Ti-5Al-5V-5Mo-3Cr alloy with single metastable  $\beta$  microstructure. *Mater. Sci. Eng. A* **2014**, *611*, 337–344. [[CrossRef](#)]
18. Zhang, H.; Shao, H.; Shan, D.; Wang, K.X.; Cai, L.L.; Yin, E.H.; Wang, Y.L.; Zhuo, L.C. Influence of strain rates on high temperature deformation behaviors and mechanisms of Ti-5Al-5Mo-5V-3Cr-1Zr alloy. *Mater. Charact.* **2021**, *171*, 110794. [[CrossRef](#)]
19. Wusatowska-Sarneck, A.M.; Miura, H.; Sakai, T. Nucleation and microtexture development under dynamic recrystallization of copper. *Mater. Sci. Eng. A* **2002**, *323*, 177–186. [[CrossRef](#)]
20. Ouyang, D.L.; Lu, S.Q.; Cui, X.; Wang, K.L.; Wu, C. Dynamic recrystallization of titanium alloy TA15 during  $\beta$  hot process at different strain rates. *Rare Metal Mater. Eng.* **2011**, *40*, 325–330.
21. Zhou, G.; Zhang, S.Q.; Zhang, H.Y.; Yu, X.M.; Liu, L.R.; Chen, L.J. Elevated temperature compression deformation behavior and mechanism of GH79 superalloy. *Rare Metal Mater. Eng.* **2019**, *48*, 3939.
22. Sellars, C.M.; Mcgeart, W.J. On the mechanism of hot deformation. *Acta Metall.* **1966**, *14*, 1136–1138. [[CrossRef](#)]
23. Zhao, J.W.; Ding, H.; Zhao, W.J.; Huang, M.L.; Wei, D.B.; Jiang, Z.G. Modelling of the hot deformation behaviour of a titanium alloy using constitutive equations and artificial neural network. *Comput. Mater. Sci.* **2014**, *92*, 47–56.
24. Liu, Y.C.; Wu, Q.; Pang, G.D.; Jiang, X.Y.; He, D.G. Hot tensile deformation mechanism and dynamic softening behavior of Ti-6Al-4V alloy with thick lamellar microstructures. *Adv. Eng. Mater.* **2019**, *22*, 1901193.

25. Wang, Z.; Wang, X.N.; Shang, G.Q.; Zhu, L.W.; Li, J.; Fei, Y.; Tian, S.; Zhu, Z.S. Study on hot deformation behavior of new high strength and toughness titanium alloy. *Rare Metal. Mat. Eng.* **2018**, *47*, 810–815.
26. Wang, Y.; Lin, D.L.; Law, C.C. Correlation between tensile flow stress and zener-hollomon factor in TiAl alloys at high temperatures. *J. Mater. Sci. Lett.* **2000**, *19*, 1185–1188. [[CrossRef](#)]
27. Prasad, Y.V.R.K. Author's reply: Dynamic materials model: Basis and principles. *Metall. Mater. Trans. A* **1966**, *27A*, 235–236. [[CrossRef](#)]
28. Balasubrahmanyam, V.V.; Prasad, Y.V.R.K. Deformation behaviour of beta titanium alloy Ti-10V-4.5Fe-1.5Al in hot upset forging. *Mater. Sci. Eng. A* **2002**, *A336*, 150–158. [[CrossRef](#)]